

The Statistics of Oceanic Turbulence Measurements. Part I: Shear Variance and Dissipation Rates

ROLF G. LUECK^a

^a *Rockland Scientific, Inc., Victoria, British Columbia, Canada*

(Manuscript received 9 February 2021, in final form 6 May 2022)

ABSTRACT: An empirically derived statistic is used to estimate the confidence interval of a dissipation estimate that uses a finite amount of shear data. Four collocated shear probes, mounted on a bottom anchored float, are used to measure the rate of dissipation of turbulence kinetic energy ϵ at a height of 15 m above the bottom in a 55 m deep tidal channel. One pair of probes measures $\partial w/\partial x$ while the other measures $\partial v/\partial x$, where w and v are the vertical and lateral velocity. The shear-probe signals are converted into a regularly resampled space series to permit the rate of dissipation to be estimated directly from the variance of the shear using $\bar{\epsilon}^L = 7.5\nu(\partial w/\partial x)^2$ (and similarly for the v component), for averaging lengths, L ranging from 1 to 10^4 Kolmogorov lengths. While the rate of dissipation fluctuates by more than a factor of 100, the fluctuations of the differences of $\ln(\bar{\epsilon}^L)$ between pairs of probes are stationary, zero mean, and distributed normally for averaging lengths of $L = \sim 30$ to 10^4 Kolmogorov lengths. The variance of the differences, $\sigma_{\ln\epsilon}^2$, scales as $L^{-7/9}$, independent of stratification for buoyancy Reynolds numbers larger than ~ 600 , and for dissipation rates from $\sim 10^{-10}$ to $\sim 10^{-5}$ W kg⁻¹. The variance decreases more slowly than L^{-1} because the averaging is done in linear space while the variance is evaluated in logarithmic space. This statistic provides the confidence interval of an ϵ estimate such as the 95% interval $CI_{95}(\epsilon) = \epsilon \exp(\pm 1.96\sigma_{\ln\epsilon})$. This result also applies to the traditional ϵ estimates that are made by way of spectral integration, after L is adjusted for the truncation of the shear spectrum.

SIGNIFICANCE STATEMENT: The results reported here can be used to estimate the statistical uncertainty of a dissipation estimate that is derived from a finite length of turbulence shear data.

KEYWORDS: Data quality control; In situ oceanic observations; Measurements

1. Introduction

The study of ocean mixing relies heavily on the estimation of the rate of viscous dissipation of turbulence kinetic energy ϵ , because it provides a means to estimate the diapycnal eddy diffusivity (Osborn 1980). Models of global circulation are sensitive to the parameterization of mixing (Wunsch and Ferrari 2004) and direct observations of ϵ are still sparse (Waterhouse et al. 2014).

The rate of dissipation is commonly derived from the measurement of the variance of microstructure shear using the air-foil shear probe, which provides one component of the fluctuation of velocity orthogonal to its direction of profiling (Osborn and Crawford 1980). A second probe mounted parallel to the other, and rotated by 90° around its longitudinal axis, provides the second cross-profile velocity component. The shear probe was developed in the 1970s (Siddon and Ribner 1965; Siddon 1971; Osborn 1974) and is now widely used for oceanic turbulence measurements. The shear probe was originally only mounted on the leading edge of freely falling vertical profilers, but is now routinely used on autonomous platforms such as self-propelled horizontal profilers (Osborn


and Lueck 1985; Goodman et al. 2006; Naveira Garabato et al. 2019), towed platforms (Fleury and Lueck 1992), on oceanic gliders (Fer et al. 2014; Palmer et al. 2015; St. Laurent and Merrifield 2017), floats (Nagai et al. 2015), and moored platforms (McMillan et al. 2016). The shear probe cannot respond to a constant cross-profile velocity. Instead, it typically measures fluctuations with frequencies higher than 0.1 Hz. The finite size of the probe limits its wavenumber resolution to 150 cpm, and this allows it to resolve fluctuations down to nearly the Kolmogorov scale, $L_K \equiv (\nu^3/\epsilon)^{1/4}$, at which viscosity dissipates the turbulence kinetic energy, for $\epsilon \lesssim 10^{-5}$ W kg⁻¹ (Macoun and Lueck 2004).

In isotropic turbulence, the rate of dissipation is related to the shear variance by

$$\epsilon = \frac{15}{2} \nu \overline{\left(\frac{\partial w}{\partial x}\right)^2} = \frac{15}{2} \nu \int_0^\infty \phi(k) dk \approx \frac{15}{2} \nu \int_0^{k_u} \phi(k) dk, \quad (1)$$

where ν is the kinematic viscosity, w is any velocity component orthogonal to the direction of profiling, x is any direction of profiling, $\phi(k)$ is the spectrum of shear, and k is the wavenumber in the x direction (Taylor 1935; Pope 2015). A statistically independent estimate of ϵ is provided by the velocity component orthogonal to w ; hence, two or more probes are usually mounted closely together on a profiler.

The increasing use of the shear probe on autonomous platforms, such as gliders and some floats, is expanding the volume of shear data that may be processed to derive dissipation rates. The potential use of shear probes on Argo floats will

 Denotes content that is immediately available upon publication as open access.

Corresponding author: Rolf Lueck, rolf@rocklandscientific.com

balloon this volume further (Roemmich et al. 2019). This renders it impractical to apply traditional quality control methods of visually inspecting the shear time series and spectra for every dissipation estimate. Data inspection and correction is important for a variety of reasons including (i) short spurious extrema due to collision with plankton, (ii) oscillations on time scales of a few seconds from jellyfish skewered by the probe, (iii) vibrations of the platform to which it is mounted, (iv) electronic noise at high wavenumbers, (v) elevated electronic noise due to poor insulation from seawater, and (vi) interference from other instrumentation.

There is currently no statistical basis for deriving the confidence interval of a dissipation estimate which can be used to identify erroneous estimates among two or more simultaneous measurements. These issues will become problematic with the increasing data volume resulting from the growing use of robotic platforms for dissipation measurements.

It is rarely possible to estimate ϵ directly from the variance of shear using the first equality in (1) because the many sources of flawed data add variance to the shear signal and they bias high this direct estimate. Instead, the variance of shear is usually estimated from the integral of its spectrum up to a finite wavenumber k_u —the approximation in (1). This method can reduce bias in the estimation of the shear variance through a judicious choice of k_u because vibrations often manifest as narrow-banded elevations of the spectrum at high wavenumbers and electronic noise resides mainly at high wavenumbers, above the inertial subrange, and often beyond the peak of the spectrum of shear. The effect of choosing a finite k_u is that the estimate of ϵ may be biased low because it does not contain all shear variance. This bias is usually corrected by comparing the measured spectrum against a model spectrum (e.g., Nasmyth 1970; Oakey 1982), to account for the excluded variance. Such model-based corrections are typically smaller than 10% but, they can be much larger when the signal to noise ratio is poor at high wavenumbers, vibrational contamination is large and not well removed, and when dissipation rates are large and the shear variance is not fully resolved because of the limited wavenumber resolution of the shear probe.

Although the usual method of spectral integration provides excellent control of the wavenumber range used to make a dissipation estimate, it provides poor control of the spatial range of an estimate because a considerable amount of data must be used to obtain a statistically reliable spectrum. On the other hand, the direct variance method, the first equality in (1), provides excellent control of the spatial scale of a dissipation estimate with nearly no control of the wavenumber range, which extends all of the way to the Nyquist wavenumber. The direct method only provides unbiased estimates of ϵ when the signal to noise ratio is very favorable and when the shear probe has the spatial resolution to completely resolve the variance of shear, i.e., $\epsilon \lesssim 10^{-5} \text{ W kg}^{-1}$.

Even when the shear data are flawless, the estimates of ϵ from two probes mounted closely together on the same platform, but measuring orthogonal velocity components, will differ due to the statistical nature of the local turbulence and the length (typically 0.5 to 5 m) of data used to estimate ϵ . The objective here is to

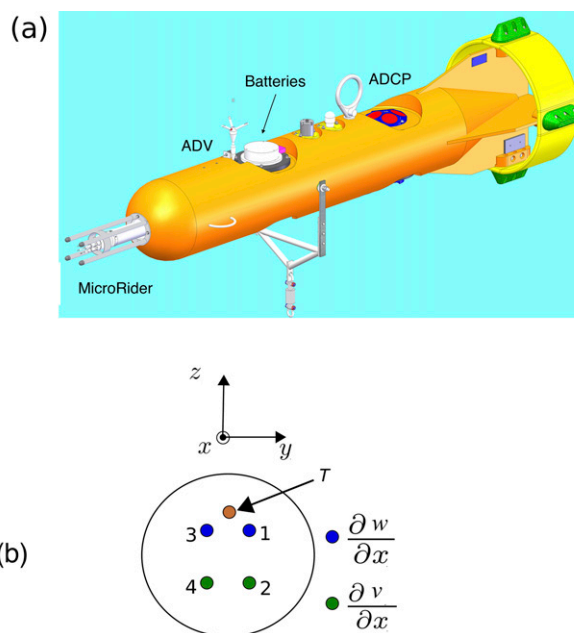


FIG. 1. (a) The Nemo float with the MicroRider shear-probe payload at its leading edge. The tips of the shear probes are 0.46 m ahead of the float, the ADV is aft of the probes by 1.20 m, and its sensing volume is 0.33 m above the hull. The batteries are aft by an additional 0.25 m. The ADCP is in the rear section. The bridle axel, a radio beacon and strobe light, and a lifting eye are near mid-body. The bridle has a swivel to allow the float to rotate around the vertical axis. The float weighs 2000 N, and has a buoyancy of 3000 N, a total length of 3.52 m, and a body (tail) diameter of 0.46 m (0.93 m). (b) A sketch of the position of the shear probes viewed from in front of the float. Their separations in the y and z directions are 0.0440 and 0.0254 m, respectively.

exploit the lognormal nature of shear variance (Gurvich and Yaglom 1967) to deduce its inherent measurement uncertainty by comparing the simultaneous rate of dissipation estimated from four shear probes that are in very close proximity (Fig. 1). Being separated by less than 0.05 m and located 15 m above the bottom, all four probes should report rates that are statistically identical. However, the estimates are made using a limited length of data, and the estimates will differ because of the statistical nature of the samples. If X_1 is a lognormally distributed random variable with a logarithmic mean of μ_1 and variance σ_1^2 , such as the shear-squared measured by one shear probe, and if X_2 is an independent and similarly distributed random variable with mean μ_2 and variance σ_2^2 , measured by a second probe in close proximity to the other, then their ratio $Z = X_1/X_2$ is also distributed lognormally, with a mean of $\mu_s = \mu_1 - \mu_2$ and a variance of $\sigma_z^2 = \sigma_1^2 + \sigma_2^2$. If the turbulence is isotropic, then $\mu_s = 0$ and $\sigma_z^2 = 2\sigma_1^2 \equiv \sigma^2$. With sufficient data, we can use the sample variance of the difference of the logarithm of ϵ estimates, from orthogonal shear-probe signals, to estimate σ^2 , determine how this variance decreases with increasing averaging length L , and derive the confidence interval of an estimate of ϵ made from a particular length of data. The variance provides the

TABLE 1. The basic deployment information for the Nemo systems in Minas Passage. The MicroRider collects 1-h-long data files, and the last three digits in their names are incremented sequentially.

| Parameter | Values |
|---------------------|-------------------------|
| Deployment | 1143:24 UTC 27 Aug 2016 |
| Recovery | 1036:36 UTC 11 Sep 2016 |
| Longitude | 64°26.310 W |
| Latitude | 45°22.149 N |
| Water depth | 55 m |
| Height above bottom | 14.8 m |
| First data file | MP2_002 |
| Last data file | MP2_360 |

uncertainty of a shear *measurement* and a quantitative criterion for identifying erroneous dissipation estimates among multiple simultaneous ones. This objective of determining the uncertainty of a measurement is distinct from that of determining the statistical nature of the variation of ϵ itself, such as how its value varies over the length and time scales associated with the forces that create and maintain turbulence in natural aquatic environments (Lozovatsky et al. 2017).

This article is structured as follows. Section 2a describes the instrumentation deployed in a highly turbulent and unstratified tidal bottom boundary layer with a moored instrument carrying four shear probes in close proximity. Section 2b describes the selection of a small subset of these data, and section 2c details the process that converts the time-domain data into a space series of shear with minimal anomalies. The probability density function (pdf) of the differences of the logarithm of dissipation estimates, for averaging lengths of 1 to 10^4 Kolmogorov lengths, is estimated in section 3, and the application of the derived pdf to the confidence interval of an ϵ estimate is presented in section 4. The results are discussed in section 5 and concluded in section 6. The pdf of a measured spectrum is presented in Lueck (2022, hereafter Part II), along with a new empirical model of the spectrum of shear.

2. Shear-probe data

a. Instrumentation

Four shear probes were mounted on the moored Nemo float and deployed for 15 days, starting on 27 August 2017, in Minas Passage located at the northern end of the Bay of Fundy, Nova Scotia, Canada (Table 1). The Nemo float (Fig. 1a) and its instrumentation are detailed in McMillan et al. (2016). It carries three instrument systems. A MicroRider (MR) is mounted on the centerline of the float at its leading edge. It provides data from four shear probes, one FP07 thermistor, a two-axis vibration sensor, a pressure transducer, a three-axis linear accelerometer, a two-axis inclinometer, and a three-axis magnetometer. The shear probes, thermistor, and vibration sensors are sampled at a rate of 2048 s^{-1} , while all others are sampled at 256 s^{-1} . The shear probes and vibration sensors are internally high-pass filtered at 0.1 Hz. A three-axis acoustic Doppler velocimeter (ADV) is mounted near the

front of the float so that its sampling volume is 0.33 m above the float. It is sampled at 4 s^{-1} and provides the current speed which is used to convert the time derivative of MR signals into along-stream (horizontal) gradients. A five-beam 1.2 MHz acoustic Doppler current profiler (ADCP) is mounted near the tail of the Nemo float. The MR and ADV are powered by separate batteries contained in a common pressure case located just aft of the ADV. The ADCP is powered by its internal battery to reduce interference with the MR data. All measurement systems record their data internally and independently. The ADV data were merged into the MR data, in postdeployment processing, after they were aligned in time using the pressure recorded by both instruments.

One-minute-averaged current speeds reached 3.8 and 2.6 m s^{-1} during the flood and ebb, respectively. The 1-min-averaged dissipation rates exceeded $1 \times 10^{-3} \text{ W kg}^{-1}$ on both phases of the tide. Consequently, the shear probes could not fully resolve the shear spectrum for the majority of their deployment, due to their limited wavenumber response of 150 cpm (Macoun and Lueck 2004). Most high-value estimates of ϵ were derived by a wavenumber regression to the shear spectrum in the inertial subrange, where it rises in proportion to $\epsilon^{2/3} k^{1/3}$. However, there were intervals of up to 25 min duration, shortly after the start of the ebb tide (current flowing to the west), when the current accelerates slowly with speeds under $\approx 1 \text{ m s}^{-1}$, dissipation rates are smaller than $\approx 10^{-5} \text{ W kg}^{-1}$, and the spectra of shear are fully resolved. During these intervals, the shear signals are strong while vibrations are relatively small because of the large mass ($\sim 400 \text{ kg}$, including entrained mass) of the float. The mooring line placed the Nemo float 14.8 m above the bottom during slack water. Current forces the float downstream of its anchor (push back) and decreases its height above the bottom (blow down). The blow down is minimal ($\leq 0.1 \text{ m}$) for currents slower than 1 m s^{-1} (McMillan et al. 2016), and thus, the data were collected from a nearly constant height above the bottom during these intervals.

b. Data selection

The MR collected 359 one hour long files, and 23 files contain segments that are useful for a statistical analysis of the directly estimated shear variance, using the first equality in (1). The selected portions of these files meet the following criteria:

- 1) current speed less than $\approx 1 \text{ m s}^{-1}$,
- 2) pitch angles within $\pm 20^\circ$,
- 3) $\epsilon \leq 10^{-5} \text{ W kg}^{-1}$,
- 4) 90% of shear variance at $k \leq 150 \text{ cpm}$,
- 5) benign vibrations for $k \leq 150 \text{ cpm}$,
- 6) approximate stationarity of ϵ estimates, and
- 7) a segment length greater than 300 m.

Speeds smaller than 1 m s^{-1} usually correspond to $\epsilon < 10^{-5} \text{ W kg}^{-1}$, low vibrations, and fully resolved shear spectra. Pitch angles smaller than $\pm 20^\circ$ assure a linear response from the shear probes. The shear probe does not fully resolve the spectrum of shear when $\epsilon \geq 10^{-5} \text{ W kg}^{-1}$, which is the value

TABLE 2. The characteristics of the segments extracted from the Nemo data files. Column 1: segment number; column 2: file number; columns 3 to 5: the smallest and largest 8 s ϵ estimates, and the upper wavenumber cutoff k_u , respectively; column 6: segment length L_0 ; columns 7 and 8: speed and heading ranges, respectively.

| Segment No. | File No. | $10^8 \epsilon_l$ (W kg $^{-1}$) | $10^8 \epsilon_h$ (W kg $^{-1}$) | k_u (cpm) | L_0 (m) | Speed (m s $^{-1}$) | Heading ($^\circ$) |
|-------------|----------|-----------------------------------|-----------------------------------|-------------|-----------|----------------------|----------------------|
| 1 | 008 | 5 | 200 | 80 | 341 | 0.3–0.5 | ± 10 |
| 2 | 009 | 1 | 1000 | 150 | 859 | 0.5–0.9 | ± 10 |
| 3 | 021 | 7 | 1000 | 150 | 956 | 0.35–0.9 | ± 8 |
| 4 | 034 | 2 | 600 | 120 | 1099 | 0.4–1.0 | ± 10 |
| 5 | 046 | 3 | 800 | 150 | 630 | 0.45–0.85 | ± 7 |
| 6 | 059 | 5 | 1000 | 150 | 1026 | 0.55–1.05 | ± 10 |
| 7 | 071 | 6 | 300 | 145 | 714 | 0.4–0.9 | ± 15 |
| 8 | 084 | 1 | 1000 | 150 | 1125 | 0.6–1.05 | ± 20 |
| 9 | 096 | 10 | 4000 | 150 | 915 | 0.3–0.8 | ± 10 |
| 10 | 195 | 7 | 1000 | 150 | 965 | 0.5–0.8 | ± 13 |
| 11 | 207 | 3 | 1000 | 150 | 1412 | 0.5–1.1 | ± 13 |
| 12 | 219 | 6 | 1000 | 150 | 832 | 0.5–0.9 | ± 12 |
| 13 | 232 | 2 | 400 | 150 | 699 | 0.55–0.7 | ± 12 |
| 14 | 244 | 2 | 1000 | 120 | 1133 | 0.4–0.9 | ± 15 |
| 15 | 256 | 40 | 500 | 150 | 884 | 0.5–0.9 | ± 10 |
| 16 | 268 | 2 | 400 | 125 | 504 | 0.45–0.8 | ± 10 |
| 17 | 281 | 3 | 200 | 115 | 603 | 0.5–0.85 | ± 8 |
| 18 | 293 | 1 | 2000 | 150 | 1011 | 0.5–0.9 | ± 10 |
| 19 | 305 | 4 | 800 | 115 | 557 | 0.4–0.65 | ± 12 |
| 20 | 318 | 6 | 400 | 140 | 388 | 0.4–0.6 | ± 15 |
| 21 | 318 | 10 | 5000 | 150 | 753 | 0.6–0.9 | ± 10 |
| 22 | 330 | 4 | 300 | 140 | 513 | 0.45–0.75 | ± 15 |
| 23 | 355 | 3 | 200 | 90 | 477 | 0.65–0.75 | ± 5 |

that is typically used to switch the estimation method from spectral integration to fitting the spectrum to $k^{1/3}$ in the inertial subrange. The fraction of the shear variance that resides at $k < 150$ cpm is judged by comparing the shear spectra against the Nasmyth spectrum, using 60 s of data. The characteristic of benign vibrations was judged qualitatively by examining the time series and spectra of the shear-probe signals. The vibrations were always small enough to be readily removed using a vibration-coherent signal removal algorithm (Goodman et al. 2006). Stationarity is considered adequate if 8 s estimates of ϵ varied by less than a decade around their median value. The natural variability of ϵ , which is likely induced by upstream topography and fluctuations of the current directions, does not allow a tighter constraint on stationarity. The selected segments must be longer than ~ 300 m to obtain a sufficient number of statistically independent samples to determine the pdf of dissipation rates when these rates are estimated using several meters of data.

The length of data extracted from the 23 selected files ranged from 700 to 1800 s, which corresponds to 340 to 1400 m, depending on the current speed (Table 2). The selected data span a total of 18.4 km, and represent approximately 10% of the data collected on this deployment. The data are reported in the frame of reference of the float for which x is forward along the major axis of the float, y points to the port side, and z is orthogonal to both and is nominally upward (Fig. 1b). Only the heading H_T is given in level-Earth coordinates—it has zero pointing east and values that increase counterclockwise looking down.

An example of the attitude of the float for a selected portion of a single file (MP2_096) indicates that the pitch $-\theta_y$

(Fig. 2b, red) is less than 20° even for speeds as low as 0.5 m s^{-1} (Fig. 2a, blue) and that the roll, θ_x (Fig. 2b, blue), variability is less than $\pm 1.5^\circ$. During an interval of 1320 s the current speed accelerates from approximately 0.5 to 0.8 m s^{-1} , which reduces the pitch angle from 18° to 8° . Throughout

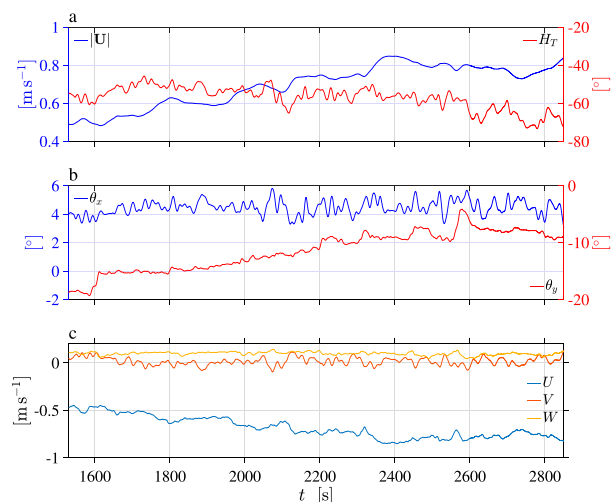


FIG. 2. Flow and float characteristics shortly after the start of an ebb. (a) Speed (blue) and geographic heading (red). (b) Right-handed rotation around the x (blue) and the y axis (red). (c) The x (U , blue), y (V , red), and z (W , gold) components of the velocity reported by the ADV in the Nemo frame of reference. The data are smoothed by the equivalent of a 16 s triangular window, except for speed which is averaged by a 64 s window.

this portion of data the heading of the float (Fig. 2a, red) varies by less than $\pm 10^\circ$. The average roll θ_x is near 4° because of a twist in the internal frame that holds the inclinometer. That is, the float is not actually rolled downward on its starboard side. The value of θ_y is not biased by the twist in the frame. The roll fluctuations (Fig. 2b, blue) are very small. However, in some of the 23 segments there are gusts that momentarily roll the float by $\approx 2^\circ$ and change its heading H_T by approximately 15° . The nominally vertical velocity W (Fig. 2c, gold) reported by the ADV fluctuates very little, compared to the cross-axis velocity V (red). The mean of W is approximately 0.1 m s^{-1} during this segment due to the slight upward pitch of the float ($\theta_y < 0$). The along-axis velocity U (Fig. 2c, blue) is always negative because the float orients itself rapidly (in less than 1 min) into the flow.

c. Data processing

The objective of the processing steps, which are detailed here, is to produce a space series of shear that can be used to estimate the rate of dissipation directly in the space domain with the first equality in (1). The sequence of processing steps that are applied to each of the 23 segments to convert the time-domain shear data into a space-domain series, and to reduced their spurious content are the following:

- 1) bandpass filtering from 0.1 to 200 Hz,
- 2) removing the vibration-coherent components in the time domain,
- 3) determining the x coordinates of the samples from the integral of the current speed,
- 4) resampling the shear and vibration data on to a uniform spacing of 2048^{-1} m ,
- 5) removing extrema due to collisions with plankton (despiking),
- 6) wavenumber-dependent boosting to compensate the spatial averaging by the shear probe,
- 7) bandpass filtering, from 0.4 cpm to a segment-dependent upper wavenumber k_u , and
- 8) scaling each shear-probe signal (by less than 2%) so that all four contain the same segment-average variance.

Bandpass filtering the data from 0.1 to 200 Hz eliminates frequency content that is outside of the range of interest, for speeds of 0.4 to $\sim 1 \text{ m s}^{-1}$ and $\epsilon \leq 10^{-5} \text{ W kg}^{-1}$, and makes it easier to visually judge the quality of the data in the time domain. Neither cutoff frequency is critical. The filtering was done by 1) taking the Fourier transform of the entire shear sequences, 2) setting to zero all components outside of the bandpass range, and 3) returning to the time domain with the inverse transform of the sequences.

Vibration-coherent content is removed in the time domain so that the times series of shear can be used to produce a space series that is free of spurious content. This time-domain process consists of using an entire segment to estimate the transfer functions that relate both vibration signals to all four shear-probe sequences from 1/4-s-long Fourier transforms of these signals. The 1/4-s-long impulse responses, which relate the shear signals to the vibration measurements, were derived from the inverse Fourier transform of the transfer functions.

There are eight impulse responses—two for each shear probe. The pair of impulse responses, for a particular shear probe, were convolved with their respective vibration signals to produce a pair of vibration-coherent signals, and these were subtracted from the shear probe signal to remove its vibration-induced content.

Removing vibration-coherent components in a shear-probe signal in the time domain produces spectra that are nearly identical to those obtained by removing vibrations in the frequency domain (Goodman et al. 2006). Quarter-second transforms were used to remove only content with frequencies higher than 4 Hz and similar results were obtained using slightly shorter and longer transforms. The transform length is not critical because little shear variance resides at frequencies smaller than 4 Hz.

Converting the data samples from the time domain into the space domain requires the along-stream position of every sample. The along-stream x coordinate of the samples was determined from the cumulative sum of the speed samples divided by their sampling rate of 2048 s^{-1} . The shear and vibration samples were then interpolated on to a uniform spatial grid using a local cubic-spline fit. A spatial grid of 2048^{-1} m was chosen so that the spatial-sampling rate is approximately commensurate with the original time-sampling rate, and to permit smoothing of the variance by as little as one Kolmogorov length, $L_K = (\nu^3/\epsilon)^{1/4} \approx 1 \times 10^{-3} \text{ m}$.

The water in the Bay of Fundy was fairly clean but collisions with plankton resulted in a small loss of data. Collisions cause extrema in the shear data that can bias their variance. Collisions are identified by comparing the absolute value of shear against a zero-phase 0.5 m smoothed version of this absolute shear. If their ratio exceeds 8, the datum is deemed anomalous, i.e., a spike. Data are replaced by a local mean for 0.02 m after, and for 0.01 m before, the spike. The data are iteratively reexamined using the same threshold of 8 until no anomalies are detected. The fraction of the shear data in a segment that was modified by the algorithm was typically 0.25% and the maximum was 0.9%.

The data were corrected for the spatial averaging induced by the shear probe by 1) taking their Fourier transform, 2) multiplying the transformed data by

$$1 + jk/50 \quad (2)$$

for wavenumbers up to 150 cpm, where k is the wavenumber, $j^2 = -1$, and the half-power response is at $k = 50 \text{ cpm}$ (Macoun and Lueck 2004), and 3) returning them to the spatial domain with the inverse Fourier transform. Such a correction is only possible in the space domain, or in the time domain during constant speed.

The data were then bandpass filtered from 0.4 cpm to a file-specific wavenumber of k_u (Table 2), using the same Fourier transform technique described in the first step of the time-domain filtering. For the dissipation rates examined here, the fraction of the variance residing below 0.4 cpm is always smaller than 0.25%. The upper wavenumber k_u was chosen to include 95% of the shear variance based on the segment-average rate of dissipation. The value of k_u depends on the rate of dissipation and ranged from 80 to 150 cpm among the segments taken

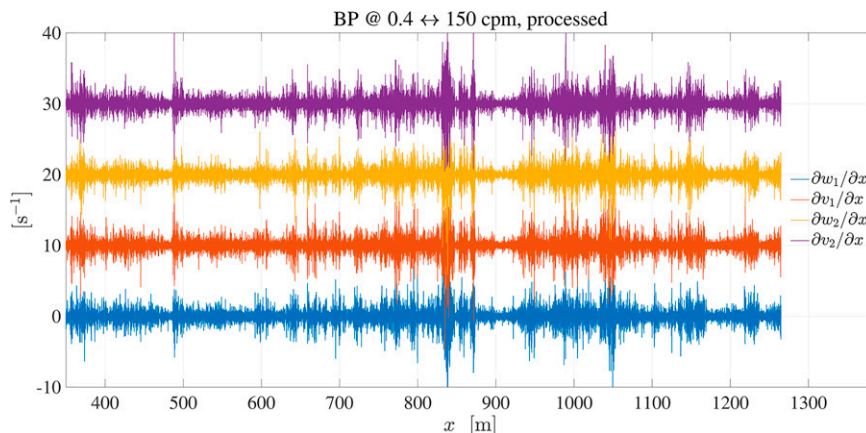


FIG. 3. An example from one segment of the shear-probe spatial data after the eight processing steps described here with an upper wavenumber of k_u (150 cpm). The zero-mean traces are offset for clarity.

from the 23 data files. This final bandpass filtering removes electronic noise residing at wavenumbers that are higher than those that contain turbulent shear and produces a nearly spurious free space series of shear (Fig. 3).

The repeatability of the calibrated sensitivity of a shear probe is within 5%, using the method of Osborn and Crawford (1980). The variance of shear is proportional to the square of the sensitivity. For each segment, the shear signals are scaled so that they all have identical variance. The scaling factors are 1 ± 0.02 , with a slight variation among the segments. The scaling is always within the $\pm 5\%$ repeatability of the shear-probe calibrations.

The validity of the data processing is checked by comparing spectra computed from the space-domain data against the spectra from nearly identical sections of the time-domain data (Fig. 4). The spectra are indistinguishable up to the cutoff wavenumber k_u (150 cpm in this example). Beyond that wavenumber, the spectra of the processed data fall rapidly (because of the bandpass filter) while the spectra of the original time-domain data flatten out and rise with increasing frequency due to electronics noise.

3. Statistics of shear-variance differences

The space-domain shear data, provided by each of the four probes, can be used to calculate the sample-by-sample (or instantaneous) “rates of dissipation” ϵ_i using

$$\begin{aligned}\epsilon_1(x) &= \frac{15}{2} \nu \left(\frac{\partial w_1(x)}{\partial x} \right)^2 \\ \epsilon_2(x) &= \frac{15}{2} \nu \left(\frac{\partial v_1(x)}{\partial x} \right)^2 \\ \epsilon_3(x) &= \frac{15}{2} \nu \left(\frac{\partial w_2(x)}{\partial x} \right)^2, \\ \epsilon_4(x) &= \frac{15}{2} \nu \left(\frac{\partial v_2(x)}{\partial x} \right)^2\end{aligned}\quad (3)$$

where the subscripts $i = 1, \dots, 4$ are the probe numbers shown in Fig. 1b. The instantaneous ϵ_i values in (3) are statistically meaningless until they are averaged over some span that is much longer than the Kolmogorov length. Averaging these ϵ values over 1000 Kolmogorov lengths (equal to 0.91 m) reveals that the local variability is large (Fig. 5a). However, even when these spatially averaged ϵ values change abruptly—often by a factor of more than 10—all four probes report nearly identical changes. The large variability of the rate of dissipation derived from an individual probe indicates that the spatially averaged values of $\bar{\epsilon}_i^L$ are highly intermittent. However, differences of their logarithm are far less intermittent than the values themselves (Fig. 5b). These differences quantify the measurement uncertainty of ϵ due to using a particular length of data.

The size of the differences $\ln \epsilon_i$ among pairs of probes will be explored for averaging lengths of 1 to 10^4 Kolmogorov lengths. However, the four shear signals are not completely

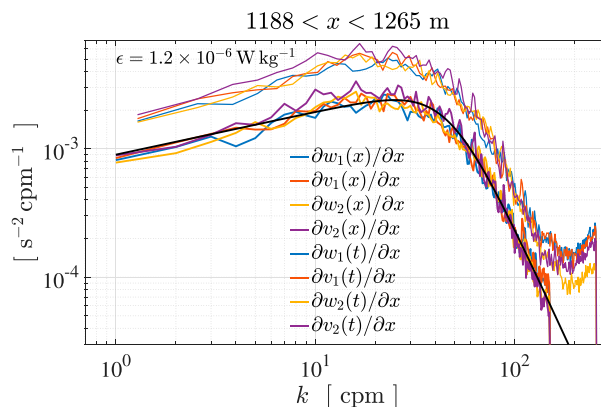


FIG. 4. Shear spectra from all four probes, for a 77 m interval of the segment shown in Fig. 3, using the space-domain data (thick lines) and the time-domain data (thin lines and raised by a factor of 2). The dimensional Nasmyth spectrum (black) for the four-probe average dissipation rate of $1.2 \times 10^{-6} \text{ W kg}^{-1}$.

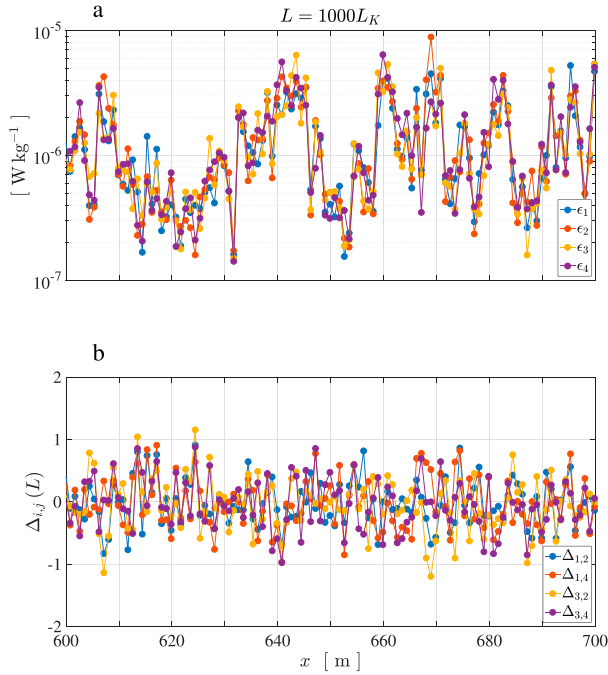


FIG. 5. (a) The four ϵ estimates using (3) and an averaging length $L = 0.91 \text{ m} = 1000L_K$, for a 100 m interval within the segment shown in Fig. 3. (b) The four differences of the logarithm of ϵ estimates for the same averaging length and interval. The differences are defined in (6).

statistically independent (Fig. 6, colored lines). Probe pairs that measure orthogonal components of the shear are incoherent for all wavenumbers and, therefore, independent (thin colored lines). On the other hand, the two pairs of probes that measure the same components of shear are partially coherent up to wavenumbers of ~ 10 cpm (thick red and green lines). However, there is little variance below 10 cpm (black line). Thus, only one of the six possible probe pairs contains two truly independent signals, such as for example w_1 and v_1 . The statistical interdependence of the (w_2, v_1) pair from the (w_1, v_1) pair can be estimated using the coherency of w_1, w_2 weighted by the wavenumber-dependent variance of either shear signal. The interdependence is

$$I_D = \frac{\int_{0.4}^{k_u} \Gamma_{w_1, w_2}^2(k) \phi_w(k) dk}{\int_{0.4}^{k_u} \phi_w(k) dk} = \int_{0.4}^{k_u} \Gamma_{w_1, w_2}^2(k) \zeta(k) dk, \quad (4)$$

where $\Gamma_{w_1, w_2}^2(k)$ is the squared coherency between shear-probe signal w_1 and w_2 (shown in Fig. 6), $\phi_w(k)$ is the spectrum of either probe, and

$$\zeta(k) \equiv \phi_w(k) / \int_{0.4}^{k_u} \phi_w(k) dk \quad (5)$$

is the shear spectrum normalized to a variance of unity. The interdependence I_D of the variance of the shear reported by

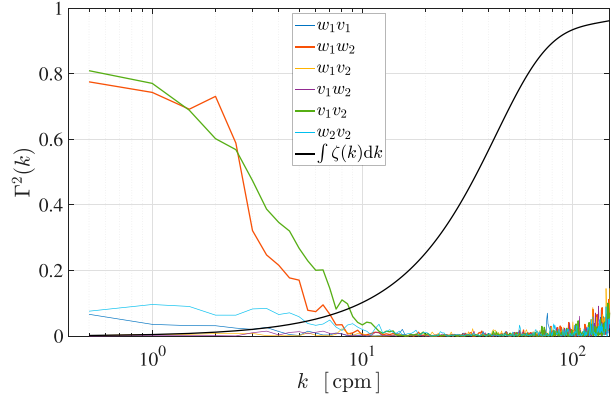


FIG. 6. The squared coherency among all possible probe pairs (colored), for the entire segment shown in Fig. 3, with thick red and green lines for the two pairs that measure the same velocity component. The fraction of variance residing below a given wavenumber (black), after the empirical model of Nasmyth using (17).

the two w probes is $\approx 2.5\%$ (Fig. 7), and this value is typical for the other segments and also for the two v probes. Their common variance resides entirely at wavenumbers smaller than 10 cpm. Thus, the pairs (w_1, v_1) , (w_2, v_1) , (w_1, v_2) , and (w_2, v_2) together provide $1 + 3 \times 0.975 = 3.9$ degrees of freedom to the estimation of the difference of the logarithm of averaged ϵ . The pairs (w_1, w_2) and (v_1, v_2) are excluded from consideration because they will bias low the estimation of the logarithmic differences, due to the coherency of identical components for $k < 10$ cpm (Fig. 6, thick lines).

Using the definitions of (3) we form the four space series

$$\Delta_{ij}(L) = \ln \bar{\epsilon}_i^L - \ln \bar{\epsilon}_j^L \quad (6)$$

for the i, j pairs of (1, 2), (1, 4), (2, 3), and (3, 4), where the $\bar{\epsilon}_i^L$ denotes a spatial average of the instantaneous dissipation rates of (3) over an interval of length L (Fig. 5b). That is, the ϵ samples of (3) are smoothed with a running average of length L , before taking their natural logarithm. If the samples

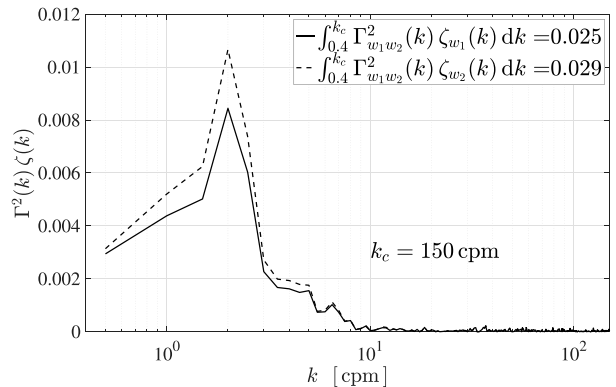


FIG. 7. The squared coherency between the signals w_1 and w_2 weighted by the spectrum of shear, and normalized by the total variance of shear, for $\partial w_1 / \partial x$ (solid) and $\partial w_2 / \partial x$ (dashed).

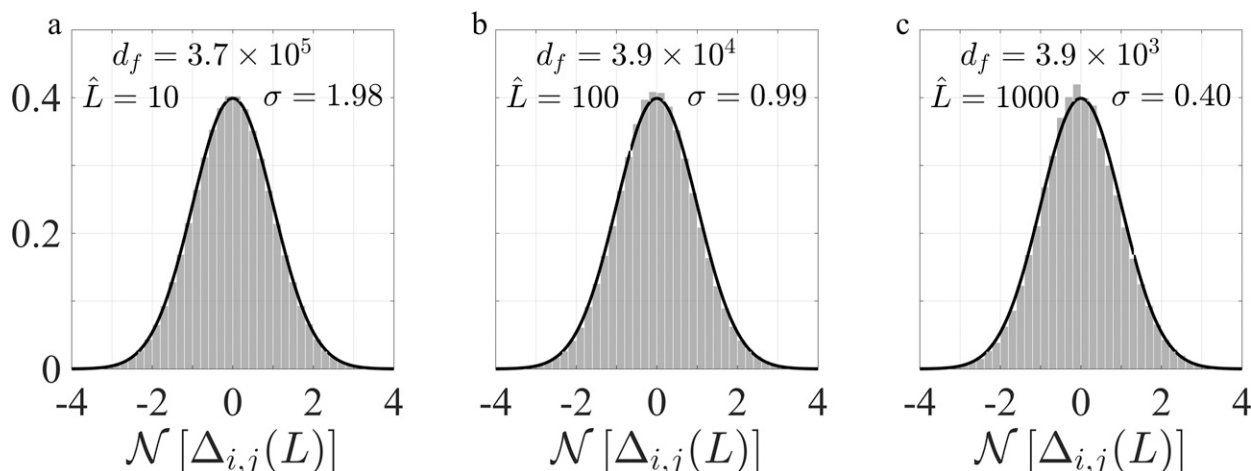


FIG. 8. The pdfs of $\Delta_{ij}(L)$, normalized by their standard deviations σ using all four probe pairs (gray) compared to a standard normal pdf (black) for averaging intervals of (a) 10, (b) 100, and (c) 10^3 Kolmogorov lengths. The Kolmogorov length is $L_K = 0.91 \times 10^{-3}$ m for this 915 m segment, and the degrees of freedom are indicated by d_f in the legend.

from the probes agree statistically, then the averages of $\Delta_{ij}(L)$ should converge to zero for all averaging length L , and the variance of $\Delta_{ij}(L)$ should decrease with increasing length L and have a value that is twice the measurement variance of single probe.

The probability density (pdf) of ϵ^L is expected to be log-normal (Gurvich and Yaglom 1967) within the restrictions outlined by Yamazaki and Lueck (1990), who found that the pdf passes a Kolmogorov–Smirnov test at the 5% level of significance when the averaging length exceeds $3 L_K$. We should expect the logarithmic difference to also be distributed normally, but with an additional restriction. The notion that the probes are simultaneously measuring the same volume of water is valid only when their separation is small compared to the averaging length. The shortest separation is 0.025 m and the longest is twice that value (Fig. 1b). The Kolmogorov length is typically 0.001 m, and therefore, averaging length shorter than ~ 50 Kolmogorov lengths may not provide a good estimate of the measurement error. Nonetheless, the pdfs of $\Delta_{ij}(L)$ are close to a normal distribution, and nearly indistinguishable, for nondimensional averaging length, $\hat{L} = L/L_K$, of 10 to 10^3 Kolmogorov lengths (Figs. 8a–c). The standard deviation of the logarithmic differences decreases with increasing averaging length. Even an averaging length of only $5L_K$ produces an empirical pdf that is indistinguishable from standard lognormal. For very long averaging lengths ($\sim 10^4 L_K$) the empirical pdf departs noticeably from a standard lognormal, mainly because of the very small degrees of freedom of such long averages. For a given segment length, L_0 , there are

$$d_f = 3.9 \left(\frac{L_0}{L} - 1 \right) \quad (7)$$

degrees of freedom in an estimate of the pdf. (The factor is 3.9 rather than 4 because of the slight interdependence of the shear signals.)

A nonparametric test of the normal distribution of $\Delta_{ij}(L)$ is provided by plotting the quantiles of the empirical cumulative density function (cdf) against the quantiles of the standard normal cdf—a q–q plot. For all 23 segments, the q–q samples pass the Kolmogorov–Smirnov (KS) test at the 5% level of significance when the averaging length exceeds 100 Kolmogorov lengths, $\hat{L} > 100$. Typically, 15% of the q–q samples fail the KS test at shorter averaging lengths, but only by a small amount. Thus, the pdfs are very close to normal for all averaging length greater than $10L_K$ (Fig. 8a). The Kolmogorov length is typically 0.001 m, and so, $\hat{L} = 100$ is about twice the largest separation of the shear probes (Fig. 1b).

The skewness of the samples,

$$S = \frac{1}{N} \sum_1^N [\Delta_{ij}(L)]^3, \quad (8)$$

where N is the total number of samples, is small and seldom exceeds 0.04. The kurtosis,

$$K = \frac{1}{N} \sum_1^N [\Delta_{ij}(L)]^4 - 3, \quad (9)$$

is almost always positive (extreme values occur more frequently than expected for a normal distribution). The value of K is typically smaller than 0.1, but can reach 0.4 for some segments, even when the samples pass the KS test.

Because the measurements from each probe are nearly statistically independent, the standard deviation of the logarithm of an ϵ estimate $\sigma_{\ln \epsilon}$ provided by any one probe is smaller than the standard deviation of the differences (6) by a factor of $1/\sqrt{2}$. That is,

$$\sigma_{\ln \epsilon} \equiv \frac{1}{\sqrt{2}} \text{STD}[\Delta_{ij}(L)] \quad (10)$$

characterizes the measurement uncertainty in a dissipation estimate as a function of data segment length. The averaging

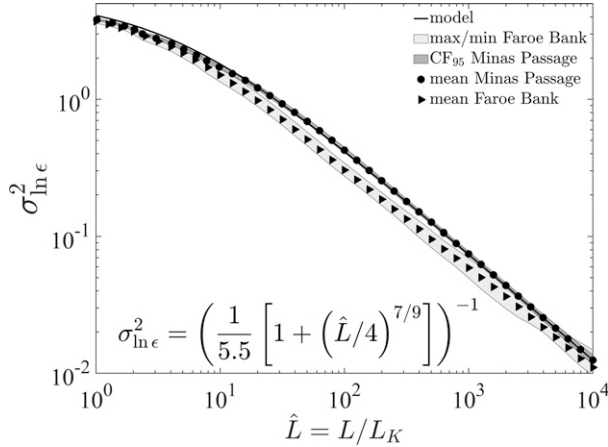


FIG. 9. The average variance of the logarithm of dissipation estimates, $\sigma_{\ln \epsilon}^2$, as a function of the nondimensional averaging length \hat{L} of all 23 segments from Minas Passage (disks), the 95% bootstrap confidence interval of these averages (dark shading), and their analytic approximation (line and text). The average variance for all 5 segments from Faroe Bank Channel (triangles) and their maximum and minimum (light shading). The Faroe Banks estimates are described in section 5.

process was applied to every one of the 23 segments (Table 2), using nondimensional averaging lengths of $\hat{L} = 1$ to 10^4 , with 10 steps per decade to examine how the standard deviation, $\sigma_{\ln \epsilon}$, depends on \hat{L} and if this standard deviation is consistent among the segments (Fig. 9, disks and dark shading). There is segment-to-segment variability, but it is small for averaging lengths shorter than $10^3 L_K$, and the bootstrap confidence interval grows slightly with increasing length due the smaller degrees of freedom for longer averaging lengths. The mean standard deviation $\sigma_{\ln \epsilon}$ at each averaging length (Fig. 9, black disks) is well represented by the solid black line given by

$$\sigma_{\ln \epsilon}^2 = \frac{5.5}{1 + (\hat{L}/4)^{7/9}}, \quad \hat{L} = \frac{L}{L_K} \approx 16 \hat{L}^{-7/9}, \quad \hat{L} \gg 4. \quad (11)$$

There is no significant difference between the average and the median of $\sigma_{\ln \epsilon}^2$ for all averaging lengths.

A small part of the scatter of $\sigma_{\ln \epsilon}^2$ may be due to a possible dissipation rate dependence. If the estimates of the standard deviations, at any one particular averaging length, are sorted according to the average ϵ of each segment, there seems to be a slight increase of variance with respect to ϵ . The scatter is large, but a least squares linear fit indicates an increase of about 10% for $\sigma_{\ln \epsilon}$ over the ϵ range from 0.2×10^{-6} to $4 \times 10^{-6} \text{ W kg}^{-1}$. A wider range must be examined to test if $\sigma_{\ln \epsilon}$ has a significant ϵ dependence.

4. Application

The empirical model of the standard deviation of a dissipation estimate (11) can be used to place a confidence interval

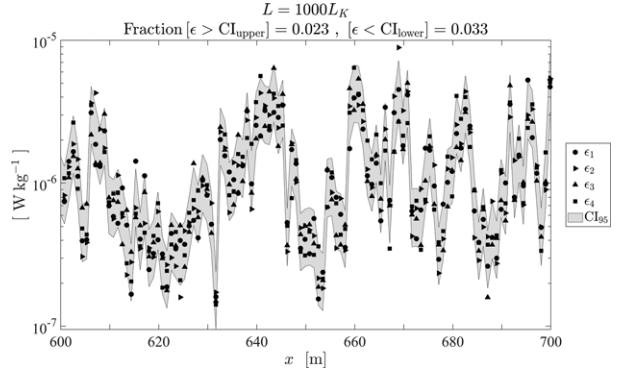


FIG. 10. The estimates of ϵ , averaged over 1000 Kolmogorov lengths, from the four shear probes (symbols) and the 95% confidence interval around their ensemble mean (gray shading) for the 100 m subsegment shown in Fig. 5a. The fraction of the estimates that fall above (below) the upper (lower) extent of the confidence interval, for the entire (915 m) segment, are given in the title.

on an ϵ estimate that is based on a specific length of data. The dissipation rate estimate itself provides a fairly good approximation of the Kolmogorov length $L_K = (\nu^3/\epsilon)^{1/4}$ because L_K is not overly sensitive to the rate. Let us start by assuming that the variance of shear is fully resolved, and later deal with partially resolved shear. Using (11) provides an estimate of $\sigma_{\ln \epsilon}^2$, and therefore, the 95% confidence interval for the logarithm of the measured dissipation rate is

$$CI_{95}(\ln \epsilon) = \ln \epsilon \pm 1.96 \sigma_{\ln \epsilon}. \quad (12)$$

That is, there is a 95% chance that the logarithm of the true rate lies within this interval. Thus, the confidence interval on ϵ itself is

$$CI_{95}(\epsilon) = \epsilon \exp(\pm 1.96 \sigma_{\ln \epsilon}). \quad (13)$$

The factor of 1.96 can be adjusted for other confidence intervals.

The confidence interval can be tested against the data. Ninety-five percent of the estimates from the probes should fall within $\exp(\pm 1.96 \sqrt{3/4} \sigma_{\ln \epsilon})$ of the four-probe average of ϵ . The factor of $\sqrt{3/4}$ accounts for the one degree of freedom that is consumed by calculating the average. That is, the individual estimates are closer to their ensemble mean than they are to the true average of ϵ (Fig. 10). For this particular segment, 2.3% of the estimates are larger than the upper limit of CI_{95} and 3.3% are below its lower limit. The observed fraction of the estimates that fall outside of the confidence limits varies among the 23 segments because of the ($\approx 16\%$) spread of the standard deviation among the segments for any particular averaging length (Fig. 11). The fraction of ϵ estimates that exceed the upper limit of CI_{95} is consistently (one exception) slightly smaller than 2.5% (squares), while the fraction that falls below this interval is usually slightly larger than 2.5% (disks). The fraction that falls outside of the complete range of CI_{95} is close to 5% and is typically between 4% and 6% (triangles). There is no discernible dependency of these

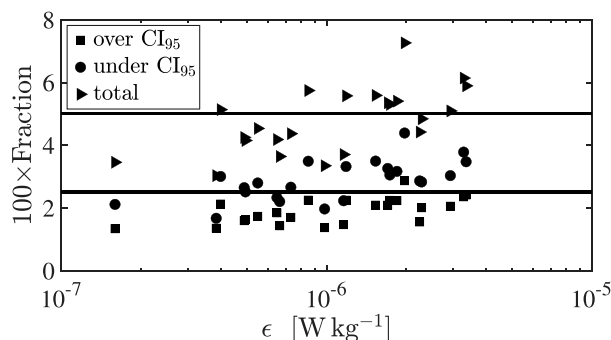


FIG. 11. The fraction of the ϵ estimates that exceed (squares), fall below (disks), and reside outside (triangles) of the confidence interval, CI_{95} , for an averaging length of $\bar{L} = 1000L_K$, for all 23 segments. The thick (thin) black line is set at 2.5% (5%).

fractions on the length of a segment (not shown) or on its mean rate of dissipation (Fig. 11).

The value of σ_{inc} can also be used to test if a pair of simultaneous estimates are different, and for outlier detection. The 95% confidence interval around the mean of a pair of ϵ estimates is $\exp(\pm 1.96 \sigma_{inc} \sqrt{1/2})$. Thus, there is only a 5% probability that a pair of estimates is separated by more than $\exp(\pm 1.96 \sigma_{inc} \sqrt{2})$. For a dissipation estimate that uses 1000 Kolmogorov lengths of data, this interval is a factor of 2.1. If a pair of estimates is separated by more than this limit, it is likely that the larger one is erroneous because any spurious measure of shear—collision with plankton, vibrations, and electronic noise—increases its variance. Rejection of an estimate should also rely on other incriminating information, such as the deviation of a spectrum from a model spectrum (e.g., the Nasmyth spectrum) and this is addressed in Part II.

In most regions where shear probes are used to estimate ϵ , the dissipation rate is less than $1 \times 10^{-5} \text{ W kg}^{-1}$, and the variance of shear is estimated from an integration of its spectrum. The integration is terminated at an upper wavenumber, k_u , that is chosen to exclude electronic and mechanical noise. However, this also excludes real shear variance. The fraction that is missed is usually estimated by a comparison to a model spectrum, such as the Nasmyth empirical spectrum, and in particular to the integral of the model spectrum up to the non-dimensional wavenumber, $\hat{k}_u = k_u(\nu^3/\epsilon)^{1/4}$. This estimation of \hat{k}_u is iterative because ϵ is initially known only approximately, but the iteration converges quickly because of its quarter-power dependency on ϵ (Lueck 2013). The main statistical implication of using less than the full wavenumber bandwidth of shear is a reduction in the degrees of freedom of the dissipation estimate because the truncation of the spectrum reduces the amount of information used in such an estimate. Therefore, the variance of a band-limited estimate is greater than the variance deduced here, (11), because of spectral truncation.

The loss of information in a spectrum that is truncated to $k_u < \infty$ can be estimated by computing the lagged autocorrelation of shear. By definition, the inverse Fourier transform of a

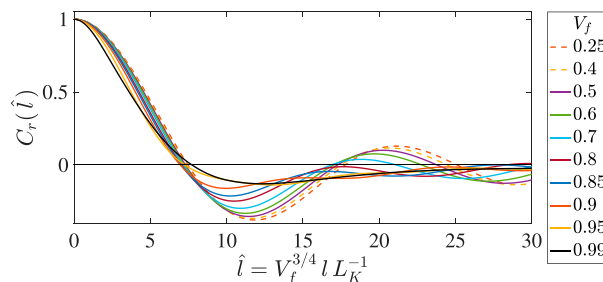


FIG. 12. The lagged autocorrelation function of the full (black) and the truncated (color) Nasmyth spectrum, where the wavenumber of truncation resolves the fraction of the total variance, V_f , indicated in the legend. The nondimensional lag lL_K^{-1} is scaled by $V_f^{3/4}$ to give all correlation functions a first zero crossing near $\hat{l} = 7$.

spectrum of shear, expressed in cyclic units, is its lagged autocovariance function,

$$C_v(l) = \frac{\overline{\partial w(x) \partial w(x-l)}}{\partial x \partial x}, \quad (14)$$

where l is the lag or spatial separation, $\partial w/\partial x$ is any one of the six possible components of shear, and the overline denotes an average. The lagged autocorrelation function (LAC) is obtained by normalizing the autocovariance function using the variance, namely,

$$C_r(l) = C_v(l) / \left(\overline{\left(\frac{\partial w}{\partial x} \right)^2} \right). \quad (15)$$

When the wavenumber of a spectrum is expressed in units of cpm, the lag l is in units of m. When this wavenumber is non-dimensionalized by the Kolmogorov length, $L_K = (\nu^3/\epsilon)^{1/4}$ (such as in the Nasmyth spectrum; Oakey 1982), then the lag is in multiples of L_K .

An often used approximation of the non-dimensional Nasmyth spectrum is

$$\Psi_{N_0}(\hat{k}) = \frac{8.05 \hat{k}^{1/3}}{1 + (20.6 \hat{k})^{3.715}}, \quad (16)$$

where $\hat{k} = k(\nu^3/\epsilon)^{1/4}$ and the wavenumber k is expressed in units of cpm. The form of (16) is close to the approximation used by Volk et al. (2002), and has the added property that its integral equals 2/15. The integral of this version of the Nasmyth spectrum, (16), is approximated to within $\pm 1\%$ by

$$I_{N_0}(\hat{k}) = \frac{15}{2} \int_0^{\hat{k}} \Psi_{N_0}(\xi) d\xi = \tanh(48 \hat{k}^{4/3}) - 2.9 \hat{k}^{4/3} \exp(-22.3 \hat{k}^{4/3}). \quad (17)$$

The lagged autocorrelation function for the Nasmyth spectrum shows a complete decorrelation at a lag of approximately seven Kolmogorov lengths (Fig. 12, black). The first zero crossing of the LAC moves to progressively larger lags as the fraction of the variance resolved gets smaller due to the

truncation of the spectrum to smaller values of \hat{k}_u . However, multiplying the lag by $V_f^{3/4}$, where V_f is the fraction of the shear variance that is resolved at the point of truncation, collapses the various LACs to nearly similar zero crossings (colored lines). This scaling works because the inverse of the decorrelation distance is proportional to the bandwidth of a spectrum and the amount of statistically independent information in a signal. For wavenumbers smaller than the peak of the spectrum, the bandwidth is k_u and grows in proportion to $V_f^{3/4}$ because of the first term on the rhs of (17). Once the upper limit of spectral integration, k_u , is beyond the peak of the spectrum, the spectrum decreases rapidly with increasing wavenumber, and very little additional information is provided by integrating the spectrum to wavenumbers well beyond the peak of the spectrum. That is, the statistically independent information available in the shear signal is exhausted once k_u is well beyond the peak of the shear spectrum. This limitation of information is naturally embodied in V_f because it has a maximum of 1. Therefore, $V_f^{3/4}$, provides a better representation of bandwidth and statistically independent information than does k_u .

Truncating a spectrum reduces the degrees of freedom of a dissipation estimate by a factor of $V_f^{3/4}$, which means that the nondimensional averaging length, L/L_K must be similarly reduced in the model of the standard deviation of a dissipation estimate (11). The model of (11) must be modified to

$$\sigma_{\text{Ine}}^2 = \frac{5.5}{1 + (\hat{L}_f/4)^{7/9}}, \quad \hat{L}_f \equiv \hat{L} V_f^{3/4} = \frac{L}{L_K} V_f^{3/4}, \quad (18)$$

where L is the dimensional length of an ϵ estimate, $L_K = (\nu^3/\epsilon)^{1/4}$ is the Kolmogorov length, and V_f is the fraction of the variance resolved by truncating the spectrum, which is computed using (17) or a similar approximation. The confidence interval of an ϵ estimate, such as (13), is then derived using the value of σ_{Ine} obtained from (18).

5. Discussion

The data examined here were collected in turbulence that is weak for tidal boundary layers but is comparatively strong for open ocean conditions where dissipation rates tend to be in the $\sim 10^{-11}$ to $\sim 10^{-7}$ W kg $^{-1}$ range. Also, the flow in Minas Passage is unstratified, but density effects should be minor if the buoyancy Reynolds number, $\epsilon/\nu N^2$, is larger than ~ 100 (Gargett et al. 1984), where N is the buoyancy frequency. It is difficult to find long datasets of nearly homogeneous conditions in the open ocean. One dataset, which is long enough to provide moderate statistical reliability, is the one collected in the main thermocline of the Faroe Bank Channel (Fer et al. 2014), above the Norwegian Sea outflow, using two shear probes mounted on a glider. Two shear probes provide only one estimate of the difference of the logarithm of ϵ .

During five profiles there were a total 4000 m of data collected in the thermocline above the outflow. The 10-m dissipation rates ranged from 1×10^{-10} to 1×10^{-7} W kg $^{-1}$ in stratification with a squared buoyancy frequency that was consistently close to $N^2 \approx 3 \times 10^{-6}$ s $^{-2}$. The profile-average buoyancy Reynolds number varied from 560 to 8000 and had

an overall average of 2500. The same processing that was applied to the data collected in Minas Passage was also applied to the thermocline data collected over Faroe Bank Channel. The standard deviation of the difference of the logarithm of the ϵ estimates from the pair of probes, σ_{Ine} , is approximately 10% smaller in these stratified conditions compared to Minas Channel (Fig. 9, triangles). The maximum and minimum of σ_{Ine}^2 is shown in light shading because the number of segments (5) is too small to allow an estimation of a bootstrap confidence interval. Thus, mild stratification ($\epsilon/\nu N^2 > \sim 600$) does not significantly change the statistical uncertainty of ϵ estimates made from shear-probe measurements.

The averaging-length dependence of the variance of the logarithm of a measurement, σ_{Ine}^2 , for example, (11) and Fig. 9, may seem peculiar because it is not proportional to \hat{L}^{-1} , and it departs from a power law for small averaging length and equals 4.1 at $\hat{L} = 1$. The departure from a power-law behavior is due to viscosity which causes the shear to be correlated for separations closer than $\hat{L} \lesssim 4$ (Fig. 12), and this correlation also makes the shear-squared interdependent at this scale. Averaging samples over a length comparable to or shorter than their decorrelation scale does not substantially reduce the variance of the averaged sequence from that of the samples themselves.

The measurement variance is not proportional to \hat{L}^{-1} for $\hat{L} \gg 4$, because the averaging is applied in linear space and σ_{Ine} is evaluated in logarithmic space. When the standard deviation is very small, $\sigma_{\text{Ine}} \ll 1$, then by virtue of the small argument approximation of an exponential, the variable is normally distributed in both linear and logarithmic space, and a running average reduces the measurement variance in proportion to the inverse of the averaging length. When σ_{Ine} is not small, averaging ϵ in linear space reduces the variance of its logarithm more slowly than \hat{L}^{-1} because a large standard deviation (logarithmic) random variable is highly skewed in linear space.

A simple simulation demonstrates that the $-7/9$ power-law averaging-length dependence of the measurement variance is determined by the intrinsic standard deviation of the logarithm of the rate of dissipation (before averaging). A pair of normally distributed sequences of length 16×10^6 , a mean of 0, and variance of 16.2, are generated to represent the logarithm of two instantaneous ϵ measurements. The sequences are smoothed with a running average of length 4 to simulate a decorrelation over this length. These smoothed values have a variance of 4.1 equaling the observed variance of σ_{Ine}^2 at $\hat{L} = 1$ (11). The exponentials of these sequences are then smoothed with a running average of lengths ranging from $N_L = 1$ to 10^4 . The variance of the logarithm of the ratio of the smoothed dissipation rates closely replicates the observed rate of decrease of σ_{Ine}^2 with increasing averaging length (Fig. 13). If the initial variance of the samples of 16.2 is increased by factors of 1.4, and 2, then the power-law exponent of the smoothed variance decreases from the observed value of -0.78 (i.e., $-7/9$), to -0.65 , and to -0.54 , respectively. Thus, σ_{Ine} , and its decrease with averaging length, may be an intrinsic property of turbulent shear, because the observed power law of $-7/9$ holds for dissipation rates spanning three factors of 10, using only Minas Passage

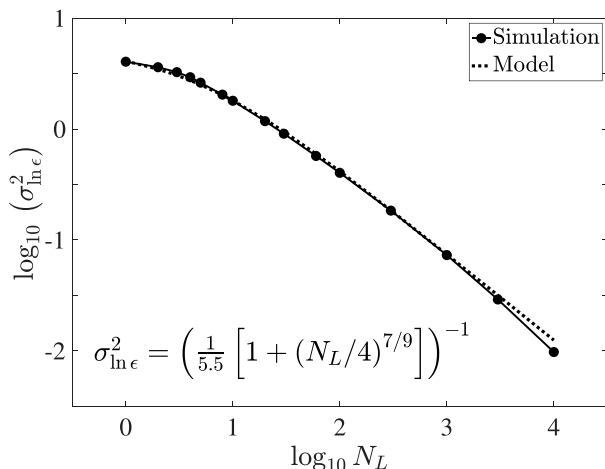


FIG. 13. A simulation of the dependence of $\sigma_{\ln \epsilon}^2$ on a running average of length N_L for a lognormal random variable (black line and disks). The dotted line is the empirical model of (11) with \hat{L} replaced with N_L .

measurements, and five factors of 10, if we include the Faroe Bank Channel measurements.

The confidence limits of a dissipation estimate computed using (13) should be expanded to include the contribution from the repeatability of the calibration of the sensitivity of the shear probe, which is currently about 5%, although this is technically a systematic error in the conversion of data into physical units, and is one that may vary slightly during usage of the probe. The calibration uncertainty produces an uncertainty of 10% in the dissipation estimate and, therefore, the confidence interval should be expanded by a factor of 1.1.

6. Conclusions

The difference of the logarithm of two, or more, simultaneous measurements of shear variance collected with sensors in close proximity has a normal probability density function (pdf), when the variance is estimated using data that spans more than ~ 10 Kolmogorov lengths. The difference is stationary even while the variance of shear measured by any one probe fluctuates by several factors of 10. The variance of the difference decreases with increasing length of data, L , used to compute the shear variance, in proportion to $\hat{L}^{-7/9}$, where $\hat{L} = L/L_K$ and L_K is the Kolmogorov length, and when $\hat{L} \geq 30$. The measurement variance of the logarithm of an individual measurement of shear variance equals one-half of the variance of the difference, as described by (11), and can be used to place confidence intervals on an estimate of shear variance and, hence, the rate of dissipation of kinetic energy by turbulence. The measurement variance can also be used to test if a pair of estimates are different.

If dissipation rates are estimated by the usual method of spectral integration, then the variance of the logarithm of the estimates must be increased by a factor of $V_f^{-3/4}$, where V_f is the fraction of the shear variance resolved by integrating the spectrum to a finite upper wavenumber, as described by (18).

The 18.5 km of data used to derive the standard deviation of a dissipation estimate, $\sigma_{\ln \epsilon}$, and its dependence on averaging length, were collected in a tidal bottom boundary layer with negligible stratification and dissipation rates $\epsilon \lesssim 10^{-5} \text{ W kg}^{-1}$. The value of $\sigma_{\ln \epsilon}$ is 10% smaller when it is derived from 4 km of data collected with a glider in the stratified thermocline over Faroe Bank Channel, where $\epsilon \lesssim 10^{-7} \text{ W kg}^{-1}$, and the buoyancy Reynolds number, $\epsilon/\nu N^2$ is in the range of ~ 600 to ~ 8000 . Moderate stratification has minimal effect on the statistical uncertainty of a dissipation estimate.

Acknowledgments. The Nemo data were kindly supplied by Alex Hay of Dalhousie University. Dave Cronkrite and Evan Cervelli of Rockland Scientific, Inc., and Richard Cheel of Dalhousie deployed and recovered the Nemo float. The Faroe Bank glider data were supplied by Ilker Fer, University of Bergen. I am grateful to the four reviewers whose huge effort provided many useful comments and suggestions. This work was partially supported by the Canadian Industrial Research Assistance Program under Project 940486.

Data availability statement. All data are available from the author.

REFERENCES

- Fer, I., A. K. Peterson, and J. E. Ullgren, 2014: Microstructure measurements from an underwater glider in the turbulent Faroe Bank Channel overflow. *J. Atmos. Oceanic Technol.*, **31**, 1128–1150, <https://doi.org/10.1175/JTECH-D-13-00221.1>.
- Fleury, M., and R. G. Lueck, 1992: Microstructure in and around a double-diffusive interface. *J. Phys. Oceanogr.*, **22**, 701–718, [https://doi.org/10.1175/1520-0485\(1992\)022<0701:MIAAAD>2.0.CO;2](https://doi.org/10.1175/1520-0485(1992)022<0701:MIAAAD>2.0.CO;2).
- Gargett, A. E. E., T. R. Osborn, and P. W. Nasmyth, 1984: Local isotropy and the decay of turbulence in a stratified fluid. *J. Fluid Mech.*, **144**, 231–280, <https://doi.org/10.1017/S0022112084001592>.
- Goodman, L., E. R. Levine, and R. G. Lueck, 2006: On measuring the terms of the turbulent kinetic energy budget from an AUV. *J. Atmos. Oceanic Technol.*, **23**, 977–990, <https://doi.org/10.1175/JTECH1889.1>.
- Gurvich, A. S., and A. M. Yaglom, 1967: Breakdown of eddies and probability distributions for small scale turbulence. *Phys. Fluids*, **10**, S59–S65, <https://doi.org/10.1063/1.1762505>.
- Lozovatsky, I., H. J. S. Fernando, J. Planella-Morato, Z. Liu, J. Lee, and S. Jinadasa, 2017: Probability distribution of turbulent kinetic energy dissipation rate in the ocean: Observations and approximations. *J. Geophys. Res. Oceans*, **122**, 8293–8308, <https://doi.org/10.1002/2017JC013076>.
- Lueck, R. G., 2013: Calculating the rate of dissipation of turbulent kinetic energy. Rockland Scientific International Tech. Note TN-028, 18 pp., <http://rocklandscientific.com/?wpdmdl=1034>.
- , 2022: The statistics of oceanic turbulence measurements. Part II: Shear spectra and a new spectral model. *J. Atmos. Oceanic Technol.*, <https://doi.org/10.1175/JTECH-D-21-0050.1>, in press.
- Macoun, P., and R. Lueck, 2004: Modelling the spatial response of the airfoil shear probe using different sized probes. *J. Atmos. Oceanic Technol.*, **21**, 284–297, [https://doi.org/10.1175/1520-0426\(2004\)021<0284:MTSROT>2.0.CO;2](https://doi.org/10.1175/1520-0426(2004)021<0284:MTSROT>2.0.CO;2).

- McMillan, J. M., A. E. Hay, R. G. Lueck, and F. Wolk, 2016: Rates of dissipation of turbulent kinetic energy in a high Reynolds number tidal channel. *J. Atmos. Oceanic Technol.*, **33**, 817–837, <https://doi.org/10.1175/JTECH-D-15-0167.1>.
- Nagai, T., R. Inoue, A. Tandon, and H. Yamazaki, 2015: Evidence of enhanced double-diffusive convection below the main stream of the Kuroshio Extension. *J. Geophys. Res. Oceans*, **120**, 8402–8421, <https://doi.org/10.1002/2015JC011288>.
- Nasmyth, P. W., 1970: Ocean turbulence. Ph.D. thesis, University of British Columbia, 69 pp.
- Naveira Garabato, A. C., E. E. Frajka-Williams, C. P. Spingys, S. Legg, K. L. Polzin, A. Forryan, and E. P. Abrahamson, 2019: Rapid mixing and exchange of deep-ocean waters in an abyssal boundary current. *Proc. Natl. Acad. Sci. USA*, **116**, 13233–13238, <https://doi.org/10.1073/pnas.1904087116>.
- Oakey, N. S., 1982: Determination of the rate of dissipation of turbulent kinetic energy from simultaneous temperature and velocity shear microstructure measurements. *J. Phys. Oceanogr.*, **12**, 256–271, [https://doi.org/10.1175/1520-0485\(1982\)012<0256:DOTROD>2.0.CO;2](https://doi.org/10.1175/1520-0485(1982)012<0256:DOTROD>2.0.CO;2).
- Osborn, T. R., 1974: Local vertical profiling of velocity microstructure. *J. Phys. Oceanogr.*, **4**, 109–115, [https://doi.org/10.1175/1520-0485\(1974\)004<0109:VPOVM>2.0.CO;2](https://doi.org/10.1175/1520-0485(1974)004<0109:VPOVM>2.0.CO;2).
- , 1980: Estimates of the local rate of vertical diffusion from dissipation measurements. *J. Phys. Oceanogr.*, **10**, 83–89, [https://doi.org/10.1175/1520-0485\(1980\)010<0083:EOTLRO>2.0.CO;2](https://doi.org/10.1175/1520-0485(1980)010<0083:EOTLRO>2.0.CO;2).
- , and W. R. Crawford, 1980: An airfoil probe for measuring turbulent velocity fluctuations in water. *Air–Sea Interaction: Instruments and Methods*, F. W. Dobson, and R. Davis, Eds., Plenum, 369–386.
- , and R. G. Lueck, 1985: Turbulence measurements with a submarine. *J. Phys. Oceanogr.*, **15**, 1502–1520, [https://doi.org/10.1175/1520-0485\(1985\)015<1502:TMWAS>2.0.CO;2](https://doi.org/10.1175/1520-0485(1985)015<1502:TMWAS>2.0.CO;2).
- Palmer, M. R., G. R. Stephenson, M. E. Inall, C. Balfour, A. Dueterhus, and J. A. M. Green, 2015: Turbulence and mixing by internal waves in the Celtic Sea determined from ocean glider microstructure measurements. *J. Mar. Syst.*, **144**, 57–69, <https://doi.org/10.1016/j.jmarsys.2014.11.005>.
- Pope, S. B., 2015: *Turbulent Flows*. Cambridge University Press, 771 pp.
- Roemmich, D., and Coauthors, 2019: On the future of Argo: A global, full-depth, multi-disciplinary array. *Front. Mar. Sci.*, **6**, 439, <https://doi.org/10.3389/fmars.2019.00439>.
- Siddon, T. E., 1971: A miniature turbulence gauge for utilizing aerodynamic lift. *Rev. Sci. Instrum.*, **42**, 653–656, <https://doi.org/10.1063/1.1685193>.
- , and H. S. Ribner, 1965: An aerofoil probe for measuring the transverse component of turbulence. *AIAA J.*, **3**, 747–749, <https://doi.org/10.2514/3.2963>.
- St. Laurent, L., and S. Merrifield, 2017: Measurements of near-surface turbulence and mixing from autonomous ocean gliders. *Oceanography*, **30** (2), 116–125, <https://doi.org/10.5670/oceanog.2017.231>.
- Taylor, G., 1935: Statistical theory of turbulence. *Proc. Roy. Soc. London*, **151A**, 421–444, <https://doi.org/10.1098/rspa.1935.0158>.
- Waterhouse, A. F., and Coauthors, 2014: Global patterns of diapycnal mixing from measurements of the turbulent dissipation rate. *J. Phys. Oceanogr.*, **44**, 1854–1872, <https://doi.org/10.1175/JPO-D-13-0104.1>.
- Wolk, F., H. Yamazaki, L. Seuront, and R. G. Lueck, 2002: A new free-fall profiler for measuring biophysical microstructure. *J. Atmos. Oceanic Technol.*, **19**, 780–793, [https://doi.org/10.1175/1520-0426\(2002\)019<0780:ANFFPF>2.0.CO;2](https://doi.org/10.1175/1520-0426(2002)019<0780:ANFFPF>2.0.CO;2).
- Wunsch, C., and R. Ferrari, 2004: Vertical mixing, energy, and the general circulation of the oceans. *Annu. Rev. Fluid Mech.*, **36**, 281–314, <https://doi.org/10.1146/annurev.fluid.36.050802.122121>.
- Yamazaki, H., and R. Lueck, 1990: Why oceanic dissipation rates are not lognormal. *J. Phys. Oceanogr.*, **20**, 1907–1918, [https://doi.org/10.1175/1520-0485\(1990\)020<1907:WODRAN>2.0.CO;2](https://doi.org/10.1175/1520-0485(1990)020<1907:WODRAN>2.0.CO;2).